ARTICLE OPEN

Check for updates

# Insights on the corrosion thermodynamics of chromium in molten LiF-NaF-KF eutectic salts

Ho Lun Chan[1]✉, Elena Romanovskaia[1]✉, Jie Qiu[2], Peter Hosemann[2] and John R. Scully[1]

The thermodynamic stability of chromium in the $Cr^0$, $Cr^{2+}$, and $Cr^{3+}$ oxidation states considering various $F^-$ ion coordination compounds was investigated in molten LiF–NaF-KF (FLiNaK) eutectic salt. Potential fluoride ion activity ($F^-$ and $CrF_3^-$) diagrams were constructed to predict the most stable Cr oxidation states as a function of anion activity, solvation state of chromium ions and potential at 600 °C. The Gibbs free energies of these compounds were estimated by utilizing a combined cyclic voltammetry – Nernst theory analysis approach in FLiNaK salt. To verify the constructed diagrams, X-ray diffraction was utilized after exposure of Cr at various applied potentials to determine whether compounds detected in solidified FLiNaK salts agreed with thermodynamic calculations. This work aims to identify key thermodynamic factors that are significant to chromium corrosion for molten salt nuclear reactor applications. The $F^-$ stability region spans the entire region where spontaneous corrosion of Cr occurs. Cr may be oxidized to $Cr^{2+}$ and $Cr^{3+}$ in the presence HF (due to moisture as an impurity) spontaneously except some conditions of $p^{1/2}H_2/a_{HF}$ etc. This situation is not changed qualitatively for various states of solvation between oxidized Cr solute in $F^-$ solvent and this aspect is substantially similar for the two cases (pair 1: $Cr^0/CrF_3^-$/ $CrF_6^{3-}$; pair 2: $Cr^0/CrF_4^{2-}/CrF_5^{2-}$) considered in this work.

*npj Materials Degradation* (2022)6:46 ; https://doi.org/10.1038/s41529-022-00251-3

## INTRODUCTION

Molten salt reactor (MSR) has been recognized as a promising system for generation IV nuclear reactor with improved safety and performance[1]. Compared to the conventional light–water reactor (LWR), molten fluoride salts (e.g., LiF–NaF–KF, LiF–$BeF_2$ eutectic) operate in the temperature range between 600 °C and 900 °C and replace water as the medium to dissolve dissolved fissile materials[1] and transfer heat; in other words, molten fluoride salts can serve as both the solvents for the reactor fuel and coolant[2,3]. The research and commercial development of MSR reactor center on solving technical problems that are deleterious to the safety and sustainability of this technology including reactor materials; and thus, the corrosion of metallic structural components should be addressed[4,5].

Fundamentally, the corrosion of metallic elements in MSRs has been posited to occur by electrochemical processes governed by mixed potential theory where the thermodynamic driving force for oxidative corrosion is determined by the difference in the Gibbs free energies of reaction between the reduction half-cell or cathodic reactions of the oxidants in the molten fluoride salts, coupled with anodic half-cell reactions associated with transition metals used in structural materials. Herein, we consider the Croxidation half-cell reactions producing oxidized chromium-fluoride compounds[6]. These are in turn based on the free energy of formation ($\Delta G_f^0$) of the relevant reactants and products. However, these free energies may vary depending upon the specific Cr oxidation states and possible $F^-$ coordination complexes that may form (e.g., $CrF_2$, $CrF_3$, $FeF_2$)[7–9]. For instance, it has recently been argued that $Cr^{2+}$ can exist as $CrF_3^-$ or $CrF_4^{2-}$ and $Cr^{3+}$ may exist as $CrF_5^{2-}$, $CrF_6^{3-}$, and $Cr_5F_{17}^{2-}$ states in molten fluorides at 700 °C[10].

The origins of the oxidants can range from moisture impurities[11] (the cause of the dissolved hydrofluoric acid corrosion[12]), dissolved cations associated with metallic elements that originally were contained in air pre-formed oxides[13], to the corrosion products themselves[11], such as reduction of Cr in $CrF_3$ or $CrF_2$ compounds originally generated from Cr metal corrosion[11,14,15]. In technological applications, corrosion may result from differences in mixed potentials established by cold legs relative to hot legs[16–19]. Chromium is a common alloying element for various candidate MSR reactor materials including alloys that exhibit good corrosion resistance in aqueous systems[4]. Since molten fluoride salt is a non-oxide forming environment with high solubility for oxygen and most oxides[9,13,20], the use of a protective $Cr_2O_3$ barrier layer is not suitable for this application[21]. This is further exacerbated by the fact that the $\Delta G_f^0$ of chromium difluorides ($CrF_2$) is lower than those of iron and nickel fluorides (other major alloying elements)[1,8], and therefore Cr is predicted to exhibit the highest thermodynamic driving force for corrosion relative to candidate oxidizers discussed above. This is evidenced by phenomena such as selective Cr dissolution along grain boundaries[7,22,23].

Nevertheless, our understanding of the electrochemical corrosion process involved with Cr metal and its alloys in the molten salt is limited. The question remains open which oxidation state ($Cr^{2+}$ or $Cr^{3+}$) is pertinent during Cr containing alloy corrosion. Thermodynamic predictions[8] suggest that Cr has a high driving force to dissolve to the $Cr^{2+}$ state due to the lower Gibbs free energy of the reaction producing $CrF_2$ (reaction 1). Direct dissolution to the $Cr^{3+}$ state (reaction 2) has not been reported as a predominant reaction step[6]. Moreover, it is posited that the resultant $Cr^{2+}$ state will then be converted to the $Cr^{3+}$ state through the disproportionation reaction (reaction 3) in which Cr metal is redeposited on its

[1]Center of Electrochemical Science and Engineering, University of Virginia, Charlottesville, VA 22903, USA. [2]Department of Nuclear Science and Engineering, University of California, Berkeley, Berkeley, CA 94720, USA. ✉email: hc4ry@virginia.edu; ggd2dr@virginia.edu

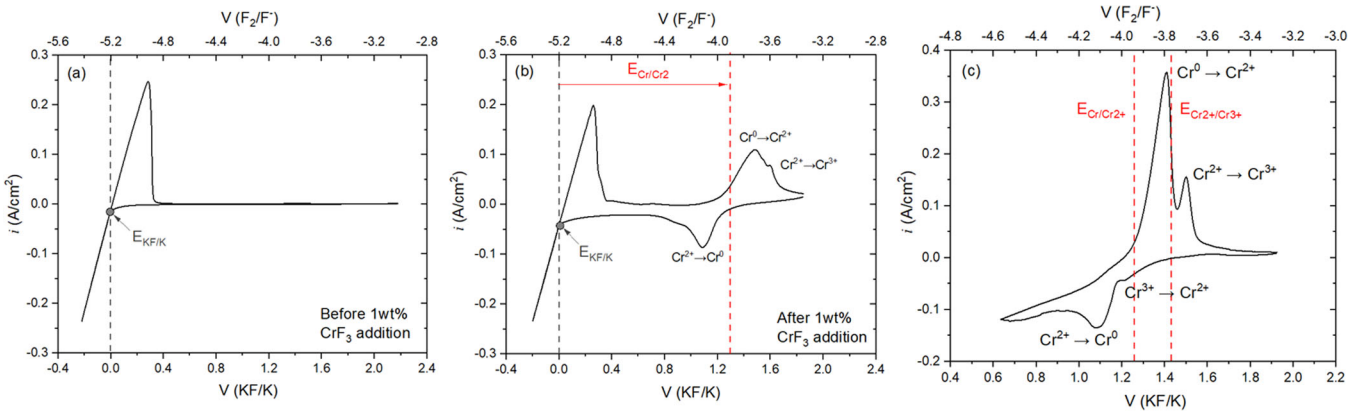


**Fig. 1 Cyclic voltammogram of Pt wire in a FLiNaK salt at 600°C.** (**a**) shows the cyclic voltammogram before and after the addition of (**b**) 1.0 wt% and (**c**) 0.42 wt% of $CrF_3$ at 600 °C. **a**, **b** indicate the equilibrium potential of KF reduction ($E_{KF/K}$). The red dotted lines in (**b**) and (**c**) show the approximate experimentally determined equilibrium redox potential of $Cr/Cr^{2+}$ redox couples ($E_{Cr/Cr}{}^{2+}$).

surface[24].

$$Cr(s) + 2F^-(ms) \leftrightarrow CrF_2(ms) + 2e^- \quad (1)$$

$$Cr(s) + 3F^-(ms) \leftrightarrow CrF_3(ms) + 3e^- \quad (2)$$

$$3CrF_2(ms) \leftrightarrow 2CrF_3(ms) + Cr(s) \quad (3)$$

where (ms) indicates a dissolved species in molten salt.

Recent progress in molten fluoride electrochemistry offers additional insights that help to interpret the corrosion mechanism of Cr. Wang et al. performed a detailed electrochemical study on a Pt wire electrode in a LiF–NaF-KF eutectic salt with the addition of $CrF_2$ at 600 °C[25]. The X-ray diffractogram of the salt mixture quenched from 600 °C revealed the presence of crystalline $CrF_3^-$ and $CrF_6^{3-}$ phases, corresponding to the chromium oxidation state of $Cr^{2+}$ and $Cr^{3+}$ ions, respectively[25]. A recent computational study by Winner et al. shows the solvated states of $CrF_3^-$ and $CrF_4^{2-}$ are possible for $Cr^{2+}$. Moreover, $CrF_5^{2-}$, $CrF_6^{3-}$, and $Cr_5F_{17}^{2-}$ are possible for $Cr^{3+}$ in molten fluorides at 700 °C[10]. However, it is unclear which solvated structure will form naturally during the spontaneous corrosion process. Nevertheless, fluoride solvation should be considered in understanding the mechanism of Cr corrosion. Thus, reactions 1–3 can be modified to reactions 4–9 through the following. It is noted that only reaction steps that involve the transfer of 1 mole of $e^-$ is considered to be the $Cr^{2+}/Cr^{3+}$ conversion reaction:

Oxidation from $Cr^0$ to $Cr^{2+}$:

$$\mathbf{CrF_3^-}: Cr(s) + 3F^-(ms) \leftrightarrow CrF_3^-(ms) + 2e^- \quad (4)$$

$$\mathbf{CrF_4^{2-}}: Cr(s) + 4F^-(ms) \leftrightarrow CrF_4^{2-}(ms) + 2e^- \quad (5)$$

Oxidation from $Cr^0$ to $Cr^{3+}$:

$$\mathbf{CrF_5^{2-}}: Cr(s) + 5F^-(ms) \leftrightarrow CrF_5^{2-}(ms) + 3e^- \quad (6)$$

$$\mathbf{CrF_6^{3-}}: Cr(s) + 6F^-(ms) \leftrightarrow CrF_6^{3-}(ms) + 3e^- \quad (7)$$

Oxidation from $Cr^{2+}$ to $Cr^{3+}$:

$$\mathbf{CrF_3^-/CrF_6^{3-}}: CrF_3^-(s) + 3F^-(ms) \leftrightarrow CrF_6^{3-}(ms) + e^- \quad (8)$$

$$\mathbf{CrF_4^{2-}/CrF_5^-}: CrF_4^{2-}(s) + F^-(ms) \leftrightarrow CrF_5^{2-}(ms) + e^- \quad (9)$$

Based on the literature, the prior approach to understand the thermodynamics of molten fluoride salt corrosion centers on (1) systematically ranking the Gibbs free energies of possible half-cell reactions ($\Delta G_r^0$) and associated half-cell reaction potentials (E)[8], and (2) developing phase stability diagrams, which depict regions of stable phases as a function of chemical compound activities (e.g., $a_{CrF2}$, $a_{CrF3}$, $a_{LiO2}$), partial pressures of oxygen ($P_{O2}$) and/or fluorine gas ($P_{F2}$), and/or potential (E)[7,11,13,26,27]. While the goal is to predict the most favorable reaction, both approaches have not considered the Cr–F solvation phenomenon reported in recent literature[10], which is critical since it affects the potential range over which thermodynamic stability of $Cr^o$, $Cr^{2+}$ and $Cr^{3+}$ is obtained. This, in turn, affects corrosion. In addition, these stability, or predominance, diagrams have limited flexibility since the oxidizing chemical potential is sometimes expressed as gaseous partial pressure (e.g., $P_{O2}$). In molten salt corrosion, it is a thermodynamic variable rather than measurable or quantitative property, making it difficult to determine the exact point which Cr locates in a phase stability, or predominance, diagram. This provides a literature gap and an opportunity to develop potential-activity diagrams that can be utilized to predict under what conditions Cr is oxidized or immune to dissolution as a function of electrode potential and fluoride ion activities (two measurable, quantitative properties) analogous to a classical Pourbaix diagram[28].

The objective of this work is to understand and predict the conditions for oxidative Cr corrosion in molten fluorides. This work aims to investigate Cr corrosion in LiF–NaF–KF (FLiNaK) eutectic salt, applicable to a MSR reactor[29]. Thermodynamic analysis was carried out based on applicatrion of the Nernst potential to predict the predominant phase of charged, solvated ions as a function of fluoride ions activity and potential (the theory is discussed in detail in "Methods"). Electrochemical measurement coupled with X-ray diffraction (XRD) were utilized to verify the predicted thermodynamic stability regions for $Cr^0$, $Cr^{2+}$, and $Cr^{3+}$ stability in FLiNaK salts at 600 °C.

## RESULTS AND DISCUSSION

### Cyclic voltammograms of Pt in FLiNaK–$CrF_3$ salts

Figure 1 shows the cyclic voltammograms on a Pt wire in FLiNaK salts with the additions of 1.0 wt% and 0.42 wt% of $CrF_3$ at 600 °C. In Fig. 1a, no Cr was present and the potassium fluoride (KF) reduction reaction was observed at the cathodic terminal of the scan, and its equilibrium potential ($E_{KF/K}$) was marked in both Fig. 1a, b. It is noted that all potential reported in this work will be referenced from this measured $E_{KF/K}$ potential value. Hence, the reference potential used in this study is a quasi-reference $E_{KF/K}$ potential. The method to obtain this value is further illustrated in "Methods". In Fig. 1c, two redox couples were observed pertaining to the $Cr/Cr^{2+}$ and $Cr^{2+}/Cr^{3+}$ redox reactions. It is noted that no particular species (e.g., $CrF_2$, $CrF_3$, $CrF_3^-$, $CrF_6^{3-}$) were assigned to describe the $Cr^{2+}$ or $Cr^{3+}$ oxidation state. The electrochemical

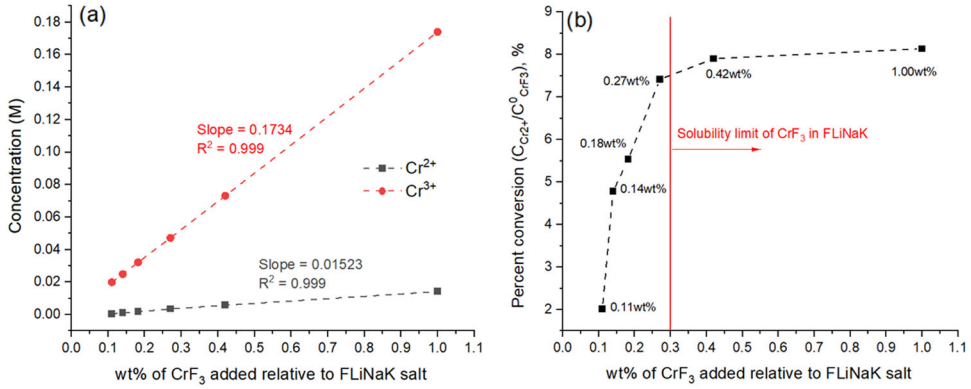


**Fig. 2 The concentration of chromium ions calculated using cyclic voltammetry results. a** Concentration of $Cr^{2+}$ and $Cr^{3+}$ species calculated based on Eqs. (18) and (19). **b** The percent conversion from $CrF_3$ to $Cr^{2+}$ species at a various weight fraction of $CrF_3$ added to FLiNaK salts. The red line marks the solubility limit of $CrF_3$ in FLiNaK reported by Yin et al.[39].

behavior of the Pt wire in FLiNaK salts with either $CrF_2$ or $CrF_3$ additions have been extensively studied by multiple authors[14,15,25,27,30]. It was reported that both redox reactions exhibit quasi-reversibility. The Nernst potential of $Cr/Cr^{2+}$ ($E_{Cr/Cr^{2+}}$) and $Cr^{2+}/Cr^{3+}$ ($E_{Cr^{2+}/Cr^{3+}}$) redox pairs may be approximated at the midpoints between the oxidation and reduction peaks[31,32], which are marked the red dotted lines in both Fig. 1b, c.

However, in Fig. 1c, it can be seen that the $Cr^{3+}/Cr^{2+}$ reduction peak was very shallow. This peak cannot be clearly distinguished for a given weight percent of $CrF_3$ added[33,34] (such as in Fig. 1b), making it difficult to precisely determine its peak potential and current. The smaller peak current and shallower peak shape may be due to the combined effects of the lower diffusivity of $Cr^{3+}$ (an order of magnitude lower than that of $Cr^{2+}$ at 600 °C in FLiNaK salts[25]), and when the reduction reaction occurs not only on the Pt surface but elsewhere in the bulk molten salt[24].

### Concentration of $CrF_2$ and $CrF_3$ in FLiNaK

Upon the addition of $CrF_3$ in FLiNaK salts, it was expected that deposited Cr particles and $CrF_2$ would be formed by the disproportionation reaction (reaction 3) as observed by Liu et al.[24] Determining the exact concentration of $CrF_2$ and $CrF_3$ in FLiNaK salts is important to the thermodynamic analysis used in the later part of this work. Given that the $Cr/Cr^{2+}$ and $Cr^{2+}/Cr^{3+}$ reactions are quasi-reversible[14,25,30,35–38], the Randles–Ševcik relation
(Eq. (10)) was used to estimate the concentration of ionic species at a known scan rate and peak current densities:

$$i_p = 0.4463nFAC_bD^{\frac{1}{2}}\left(\frac{nFv}{RT}\right)^{1/2} \quad (10)$$

where $i_p$ is the peak current density; n is the moles of electrons transferred; A is the area; $C_b$ is bulk concentration; v is the scan rate; D is the diffusivity; R is the university gas constant 8.314 J $K^{-1}$ $mol^{-1}$; *T* is temperature To approximate the concentration of $Cr^{2+}$ species in our FLiNaK–$CrF_3$ salt, the ratio of peak current densities associated with $Cr/Cr^{2+}$ and $Cr^{2+}/Cr^{3+}$ reactions were determined, yielding:

$$\frac{C_{Cr2+}}{C_{Cr3+}} = \frac{i^{peak}_{Cr/Cr2+}}{i^{peak}_{Cr2+/Cr3+}}\left(\frac{D_{Cr3+}}{D_{Cr2+}}\right)^{1/2} \quad (11)$$

where $i^{peak}_{Cr/Cr2+}$ and $i^{peak}_{Cr2+/Cr3+}$ are the peak current densities in the CV associated with the $Cr/Cr^{2+}$ and $Cr^{2+}/Cr^{3+}$ oxidation peaks, and $D_{Cr^{2+}}$ and $D_{Cr^{3+}}$ are the diffusivities of $Cr^{2+}$ and $Cr^{3+}$ related species, which were reported by Wang and Zhang[25] to be $2.55 \times 10^{-5}$ and $7.74 \times 10^{-6}$ $cm^2$ $s^{-1}$ in FLiNaK salts at 600 °C. Using the disproportionation reaction (3) as the basis for stoichiometric conversion, the resulting ratio of $Cr^{2+}$ to $Cr^{3+}$ concentration when $Cr^{3+}$ is added can also be expressed as:

$$\frac{C_{Cr2+}}{C_{Cr3+}} = \frac{3x}{C^0_{CrF_3} - 2x} \quad (12)$$

where x represents the moles reacted. Using Eqs. (11) and (12), the concentration of $Cr^{2+}$ and $Cr^{3+}$ species as a function of initial $CrF_3$ concentration ($C^0_{CrF_3}$) can be obtained as shown in Fig. 2a. Both $Cr^{2+}$ and $Cr^{3+}$ species follow a linear relationship with $C^0_{CrF3}$ as shown in Eqs. (13) and (14):

$$C^{2+}_{Cr}(M) = 0.0152\, C^0_{CrF_3}(wt\%) \quad (13)$$

$$C^{3+}_{Cr}(M) = 0.173\, C^0_{CrF_3}(wt\%) \quad (14)$$

The percent conversion of initial $CrF_3$ to $Cr^{2+}$ species was computed and shown in Fig. 2b. The red line marks the solubility limit of $CrF_3$ in FLiNaK salts, which was calculated to be 0.3 wt% by Yin et al.[39]. Prior to $CrF_3$ saturation, the percent conversion increased and plateaued when 0.42 wt% of $CrF_3$ was introduced, which is consistent with thermodynamic prediction[39]. Upon saturation, it was determined that about 7.71% of $CrF_3$ was

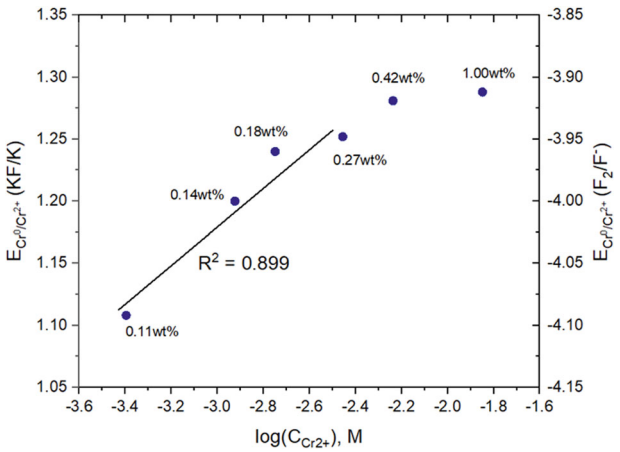


**Fig. 3 The Nerst potentials associate with $Cr^0/Cr^{2+}$ redox reaction at different calculated concentrations of $Cr^{2+}$ ions in FLiNaK at 600 °C.** The left *y*-axis shows the potential relative to the pseudo KF/K potential and the right y-axis shows that calculated potential referenced to the $F_2/F^-$ potential.

converted to $CrF_2$, close to the percent conversion value reported by Peng et al.[36].

### Estimating the Gibbs free energy of formation of solvated chromium fluorides

Figure 3 shows the experimental $Cr/Cr^{2+}$ Nernst potential ($E_{Cr/Cr^{2+}}$) indicated by symbols versus the calculated $Cr^{2+}$ concentration (Eq. (13)) on a logarithmic scale. The solid line is a fit to the data that can be fitted against Eq. (15). Between 0.11 and 0.27 wt% $CrF_3$ addition, the $E_{Cr/Cr^{2+}}$ potential exhibits a positive linear relationship with the log-scale concentration, which is consistent with the general Nernst expression of the ($Cr \rightleftharpoons Cr^{2+} + 2e^-$) half-cell redox reaction:

$$E_{Cr/Cr^{2+}} = E^0_{Cr/Cr^{2+}} + \frac{2.303RT}{2F}\log(a_{Cr^{2+}}) \quad (15)$$

$$E_{Cr/Cr^{2+}} = E^0_{Cr/Cr^{2+}} + \frac{2.303RT}{2F}\log(\gamma_{Cr^{2+}}) + \frac{2.303RT}{2F}\log(C_{Cr^{2+}}) \quad (16)$$

At 0.42 wt% and 1.00 wt%, the $E_{Cr/Cr^{2+}}$ potentials measured were similar. This was likely related to the saturation of $CrF_3$ in FLiNaK when concentrations greater than the solubility limit of 0.3 wt% of $CrF_3$ was introduced[39], resulting in the formation of distinct $K_2CrF_5$ or $K_3CrF_6$ phases in FLiNaK[39]. When the solubility limit is exceeded, the FLiNaK salt remains at a constant relative concentration of $Cr^{2+}$ and $Cr^{3+}$ in the FLiNaK salts, in which case the measured $E_{Cr/Cr^{2+}}$ potential values will not change.

The linear region in Fig. 3 can be fitted and extrapolated to determine the standard electrode potential ($E^0_{Cr/Cr^{2+}}$) using the *y*-intercept of Eq. (16). Using a similar electrochemical approach[27], Massot et al. reported that $\gamma_{Cr^{2+}}$ (activity coefficient of $Cr^{2+}$) to be close to unity in LiF–NaF salts at 700 °C[27]. In this work, $E^0_{Cr/Cr^{2+}}$ was found to be −3.41 $V_{F_2/F^-}$, which is similar to −3.35 $V_{F_2/F^-}$ the pure compound reference state value of $CrF_2$ from the thermochemical database (HSC Chemistry software 6.1)[27]. Using Eqs. (17) and (18) to relate $E^0_{Cr/Cr^{2+}}$ to $\Delta G^0_f$ of $Cr^{2+}$, the $\Delta G^0_f$ of $Cr^{2+}$ was calculated to be −657.7 kJ/mol $F^-$, which is similar to the literature value of $\Delta G^0_f$ of $CrF_2$ reported in Table 1[40].

$$\Delta G^0 = -nF\Delta E^0_{Cr/Cr^{2+}} \quad (17)$$

$$\Delta G^0 = \Delta G^0_f(Cr^{2+}) - \Delta G^0_f(Cr) \quad (18)$$

In molten fluorides, the $Cr^{2+}$ oxidation state can also possibly exist in the forms of $CrF_3^-$ or $CrF_4^{2-}$ species[10]. To obtain their $\Delta G^0_f$ values, the half-cell redox reactions of $Cr/CrF_3^-$ and $Cr/CrF_4^{2-}$ were first separately considered. To determine the precise $E^0_{Cr/Cr^{2+}}$ standard electrode potentials pertaining to the $Cr/CrF_3^-$ ($E^0_{Cr/CrF_3^-}$) and $Cr/CrF_4^{2-}$ ($E^0_{Cr/CrF_4^{2-}}$) solvated states, we can consider the Nernst expression for reactions 4 and 5:

$$E_{Cr/CrF_3^-} = E^0_{Cr/CrF_3^-} + \frac{2.303RT}{2F}\log\left(\frac{a_{CrF_3^-}}{a^3_{F^-}}\right) \quad (19)$$

$$E_{Cr/CrF_4^{2-}} = E^0_{Cr/CrF_4^{2-}} + \frac{2.303RT}{2F}\log\left(\frac{a_{CrF_4^{2-}}}{a^4_{F^-}}\right) \quad (20)$$

**Table 1.** Standard Gibbs free energy of formation ($\Delta G^o_f$) of potassium fluoride and chromium-fluoride compounds at 600 °C.

| Compound | KF | $CrF_2$ | $CrF_3$ | Ref. | Note |
|---|---|---|---|---|---|
| $\Delta G_f^0$ (kJ/mole) | −479.54 | −660.6 | −973.67 | Barin[40] | Uncorrected |
| | −473.63 | −656.3 | −969.43 | – | Supercooled corrected |

Assuming that (i) the activity coefficient of $Cr^{2+}$ ions in FLiNaK salts is unity[8,27], (ii) the activity coefficient of $F^-$ ions is unity in FLiNaK salt since the $F^-$ ions do not form complexes or a separate phase with $Li^+$, $Na^+$ and $K^+$ ions[8,9,41], (iii) and the concentration of $F^-$ ions is 49.3 M based on stoichiometric calculation (i.e., log ($a_{F^-}$) = 1.693). The intercept of Eq. (16) can be related to that in Eqs. (19) and (20), resulting in the relations:

$$E^0_{Cr/CrF_3^-} = E^0_{Cr/Cr^{2+}} - 0.435 \quad (21)$$

$$E^0_{Cr/CrF_4^{2-}} = E^0_{Cr/Cr^{2+}} - 0.580 \quad (22)$$

Using these relations, the formal potentials of each $Cr^{2+}$ solvated species may be estimated. The integers presented in Eqs. (21) and (22) are a function of the stoichiometric moles of $F^-$ ions consumed, which is different depending on the solvated structure. For clarity purposes, the calculation of these standard potentials assumes that only one solvated state contributes to the $Cr/Cr^{2+}$ redox reaction. In this work, the $E^0_{Cr/CrF_3^-}$ and $E^0_{Cr/CrF_4^{2-}}$ are found to be −3.848 and −3.994 $V_{F_2/F^-}$, which are equivalent to the $\Delta G^0_f$ values of −742.6 and −770.9 kJ/mol, respectively.

The method presented relies on identifying both the oxidation and reduction potentials of a redox reaction. However, it was previously mentioned that the reduction peak of $Cr^{3+}/Cr^{2+}$ was shallow, and could yield erroneous Nernst potentials.Therefore, the experimental–theoretical method utilized above may not yield reliable result when estimating the $\Delta G^0_f$ of $CrF_5^{2-}$ and $CrF_6^{3-}$ species in this case.

An alternative approach was used. With UV-Vis absorption spectroscopy[24] correlated with cyclic voltammetry measurements[36], it was reported that the $Cr^{2+}$ and $Cr^{3+}$ states can coexist in equilibrium, saturated condition, upon the addition of $CrF_2$ or $CrF_3$ salts in FLiNaK. In Fig. 2b, it was found that 7.71% of $Cr^{3+}$ was converted to $Cr^{2+}$ species, which is similar to the value reported by Peng et al.[36] and Zhang et al.[25]. Upon $CrF_3$ saturation, it is fair to assume that the ratio of $Cr^{2+}/Cr^{3+}$ activities (i.e., $a_{CrF_3^-}/a_{CrF_6^{3-}}$ or $a_{CrF_4^{2-}}/a_{CrF_5^{2-}}$) were 0.0814.

Consider the Nernst equations for reactions 8 and 9:

$$E = E^0 + \frac{2.303RT}{F}\log\left(\frac{a_{CrF_6^{3-}}}{a_{CrF_3^-}a^3_{F^-}}\right) \quad (23)$$

$$E = E^0 + \frac{2.303RT}{F}\log\left(\frac{a_{CrF_5^{2-}}}{a_{CrF_4^{2-}}a_{F^-}}\right) \quad (24)$$

With a $Cr^{2+}/Cr^{3+}$ equilibrium activity ratio of 0.0814 and log($a_{F^-}$) of 1.693, Eqs. (23) and (24) can be simplified to the forms:

$$E^0_{CrF_6^{3-}/CrF_3^-} = E_{CrF_6^{3-}/CrF_3^-} + 0.690 \quad (25)$$

$$E^0_{CrF_5^{2-}/CrF_4^{2-}} = E_{CrF_5^{2-}/CrF_4^{2-}} + 0.104 \quad (26)$$

In this case, the standard or formal potentials of reactions 8 and 9 can be experimentally determined by measuring the redox potential of $E_{Cr^{2+}/Cr^{3+}}$ when FLiNaK salt is saturated with $CrF_3$. In this work, $E_{Cr^{2+}/Cr^{3+}}$ was found to be +1.43 $V_{KF/K}$ or −3.77 $V_{F_2/F^-}$. $E^0_{CrF_6^{3-}/CrF_3^-}$ and $E^0_{CrF_5^{2-}/CrF_4^{2-}}$ were found to be −3.081 and −3.667 $V_{F_2/F^-}$, respectively. Using Eq. (18) and the $\Delta G^0_f$ values of $CrF_3^-$ and $CrF_4^{2-}$ previously determined, the $\Delta G^0_f$ of $CrF_5^{2-}$ and $CrF_6^{3-}$ were calculated to be −1124.7 and −1039.9 kJ/mol, respectively. The summary of the $\Delta G^0_f$ of solvated chromium fluorides is shown in Table 2. It is noted that Eqs. (21) and (22) were used to calculate the $\Delta G^0_f$ in the case of solvated $CrF_3^-$ or $CrF_4^{2}$ species using data presented by Massot et al.[27]. The result of this work yields a similar value as compared in Table 2.

**Table 2.** Calculated standard Gibbs free energy of formation ($\Delta G_f^0$) of solvated chromium-fluoride compounds based on cyclic voltammetry results at 600 °C.

| Solvated state | $CrF_3^-$ ($Cr^{2+}$) | $CrF_4^{2-}$ ($Cr^{2+}$) | $CrF_5^{2-}$ ($Cr^{3+}$) | $CrF_6^{3-}$ ($Cr^{3+}$) | Ref. |
|---|---|---|---|---|---|
| $\Delta G_f^0$ (kJ/mole) | −742.6 | −770.9 | −1124.7 | −1039.9 | This work |
| | −733.4[a] | −761.7[a] | – | – | Massot et al.[27] |

[a]The Gibbs free energy of solvated chromium fluorides reported here were derived from the formal potential ($E^0_{CrF2/Cr}$) reported by Massot, 2021 using Eqs. (21) and (22) in this work.

### Stability of $Cr^{2+}$ and $Cr^{3+}$ in molten fluorides

The Nernst equations for key redox reactions involving $CrF_3$, $CrF_3^-$, $CrF_4^{2-}$, $CrF_5^{2-}$, $CrF_6^{3-}$, and Cr species are listed in Table 3. The predominance region of each possible reaction product considered in Table 4 is plotted as a function of potential versus the $F^-$ (Fig. 4) and the $CrF_3^-$ (Fig. 5) activities on a logarithmic scale. The solid lines indicate equilibrium boundaries between the species considered. Given the complexity arising from the consideration of all solvated states, two pairs of solvated species (pair 1: $Cr^0$/$CrF_3^-$/$CrF_6^{3-}$; pair 2: $Cr^0$/$CrF_4^{2-}$/$CrF_5^{2-}$) were first independently considered.

Figure 4a, b illustrates the potential log($a_F^-$) diagrams for pair 1: $Cr^0$/$CrF_3^-$/$CrF_6^{3-}$ (Fig. 4a) and for pair 2: $Cr^0$/$CrF_4^{2-}$/$CrF_5^{2-}$ (Fig. 4b) species in molten fluorides at 600 °C. The activities of all Cr ionic species were assumed be $10^{-6}$ M. All potentials displayed are with respect to the evolution of fluorine gas ($F_2/F^-$), whose potential value is calculated from the Nernst equation of reaction 27 (Table 3). The red vertical line at log($a_F^-$) = 1.693 indicates the fluoride activity corresponding to the FLiNaK salts. The blue and orange dashed line indicates the potential window of molten FLiNaK salts defined by reactions 27 and 28. The black dotted-dash line indicates the HF reduction reaction (reaction 29) at the various ratios of $p^{1/2}_{H2}/a_{HF}$:

$$KF(ms) + e^- \leftrightarrow K(s) + F^-(ms) \quad (27)$$

$$2F^-(ms) \leftrightarrow F_2(g) + 2e^- \quad (28)$$

$$HF(ms) + e^- \leftrightarrow \frac{1}{2}H_2(g) + F^-(ms) \quad (29)$$

In Fig. 4a, the $CrF_3^-$ ions exist in a relatively narrow stability region, ~150 mV wide at the FLiNaK salt composition (red line). Above −3.284 $V_{F_2/F^-}$, the $CrF_6^{3-}$ species (+2 oxidation state) is predicted to be most thermodynamically stable. This behavior remains consistent in the range of log($a_{F^-}$) studied. It is also noted that the equilibrium potential given by the Nernst potential for hydrogen evolution (reaction 29) exists at potentials above that $CrF_3^-$/$CrF_6^{3-}$ oxidation reaction (8), indicating the oxidizing power of HF towards spontaneous anodic dissolution of Cr leading to formation of solvated $Cr^{2+}$ and $Cr^{3+}$. In Fig. 4b, the stability regions of Cr, $CrF_4^{2-}$, and $CrF_5^{2-}$ species are shown. As the log ($a_F^-$) increases, the stability region of $CrF_4^{2-}$ species widens, and then oxidized to $CrF_5^{2-}$ through reaction 9. To verify which one of these situations actually exists when Cr is exposed to FLiNaK systems at 600 °C, high purity Cr was potentiostatically polarized to −5, −4, −3.2 $V_{F_2/F^-}$ in FLiNaK salts at the same temperature (marked as the green, blue, red dots in Fig. 4). The composition of the solidified residual salts was analyzed with XRD. This will be discussed in the next section.

Figure 4 predicts that Cr would remain as the $Cr^0$ state (in the "immunity" region) when it is polarized at or below −5 $V_{F_2/F^-}$, and undergo active corrosion to either $CrF_3^-$ or $CrF_5^{2-}$ state at −4 $V_{F_2/F^-}$, and either $CrF_5^{2-}$ or $CrF_6^{3-}$ state at −3.2 $V_{F_2/F^-}$. Potentiostatic hold experiments coupled with XRD were used to verify these predictions. Figure 5 shows the XRD of FLiNaK salts after Cr was potentiostatically polarized to −3.2 $V_{F_2/F^-}$ for 50 h, −4 $V_{F_2/F^-}$ for 50 h, and −5 $V_{F_2/F^-}$ for 1 h.

In the pure solidified FLiNaK (Fig. 5a), the XRD patterns reveal diffraction peaks of KF, LiF and NaF with KF peaks sharing the highest percent intensity. When Cr metal was held at −5 $V_{F_2/F^-}$ for 1 h, no significant mass loss of Cr was observed. However, the XRD pattern (Fig. 5b) of the tested salts shows low-intensity diffraction peaks corresponding to the presence of $NaCrF_3$ (peak 4) and $KCrF_3$ (peak 9) species. The presence of Cr may be attributed to the dissolution of a native $Cr_2O_3$ oxide film at the beginning of the experiment. It is noted that large cathodic reduction current density (>1 A/cm$^2$) was observed after 1 h of potentiostatic hold (not shown) at this potential. This may either be due to formation of H2 bubbles from HF reduction or the reduction of potassium on the Cr surface.

Figure 5c, d shows the XRD patterns of FLiNaK salts where a Cr coupon was potentiostatically polarized at −4 $V_{KF/K}$ or −3.2 $V_{F_2/F^-}$ for 50 h, respectively. In Fig. 5c, the presence of $NaCrF_3$ (peak 4) and $KCrF_3$ (peak 9) species were identified, corroborating with thermodynamic prediction. In Fig. 5d, the $NaCrF_3$ (peak 4), $KCrF_3$ (peak 9), $K_2NaCrF_6$ (peak 7), $K_3CrF_6$ (peak 8), $Li_2NaCrF_6$ (peak 10) compounds were identified, confirming the existence of both $CrF_3^-$ and $CrF_6^{3-}$ states. The $CrF_3^-$ likely formed during the solidification of FLiNaK and maintained a thermodynamic equilibrium with the $CrF_6^{3-}$ state[24]. The $K_2NaCrF_6$, $K_3CrF_6$, $Li_2NaCrF_6$ compounds suggest that the $Cr^{3+}$ ion has a coordination number 6 at the temperature studied.

Results obtained are in a good correlation with literature data and previous work on compound prediction reported in Ab-initio simulations[10]. In all potentials studied, no $CrF_5^{2-}$ related compounds were detected. This indicates that the Cr/$Cr^{2+}$ and $Cr^{2+}$/$Cr^{3+}$ seen in Fig. 1 likely correspond to the Cr/$CrF_3^-$ and $CrF_3^-$/$CrF_6^{3-}$ redox couples.

During the corrosion of Cr, the activities of $CrF_3^-$ and $CrF_6^{3-}$ species in the FLiNaK salts are expected to increase over an exposure period. Therefore, it is useful to consider the change in thermodynamic driving forces (Table 3) with respect to the activities of $CrF_3^-$ and $CrF_6^{3-}$ ions under a defined constant of log ($a_F^-$) where (log(49.3) = 1.693 for FLiNaK).

Figure 6 shows the potential-activity diagrams considering the predominant phases of Cr, $CrF_3^-$, and $CrF_6^{3-}$ species as a function of log($a_{CrF3}^-$) and potential. The equilibrium potential between Cr and $CrF_3^-$ ions was computed from reaction 4 and exhibits a linear relationship with log($a_{CrF3}^-$). The blue circular symbols shown in Fig. 6 are the experimental half-cell Nernst potential reported in Fig. 3, which are closely follow but slightly different from the thermodynamic predictions. Nevertheless, the boundary of these stability regions is sensitive to the $\Delta G_f^0$ of solvated chromium fluorides (Table 2) utilized to construct these potential-activity diagrams. The use of cyclic voltammetry provides a relatively straightforward method to estimate these $\Delta G_f^0$ values, but the method is sensitive to errors. For example, the uncertainties could be related to the use of quasi $E_{KF/K}$ potential, temperature distributions or natural convection effects during molten salt electrochemistry measurement or because the Nernst potential

**Table 3.** Equilibrium redox reactions and their thermodynamic expression utilized for the construction of potential concentration diagrams in molten fluoride salts.

| Description | Reaction # | Chemical equation | Nernst equation/Gibbs free energy expression |
|---|---|---|---|
| Potential window for molten fluorides | 27 | $KF + e^- \leftrightarrow K + F^-$ | $E = E^0 - \frac{2.303RT}{F}\log(\frac{a_{F^-}}{a_{KF}})$ |
| | 28 | $F_2 + 2e^- \leftrightarrow 2F^-$ | $E = E^0 - \frac{2.303RT}{2F}\log(\frac{a_{F^-}^2}{p_{F_2}})$ |
| Direct dissolution from $Cr^0$ to $Cr^{2+}$ | 4 | $Cr + 3F^- \leftrightarrow CrF_3^- + 2e^-$ | $E = E^0 + \frac{2.303RT}{2F}\log\left(\frac{a_{CrF_3^-}}{a_{F^-}^3}\right)$ |
| | 5 | $Cr + 4F^- \leftrightarrow CrF_4^{2-} + 2e^-$ | $E = E^0 + \frac{2.303RT}{2F}\log\left(\frac{a_{CrF_4^{2-}}}{a_{F^-}^4}\right)$ |
| Direct dissolution from $Cr^0$ to $Cr^{3+}$ | 6 | $Cr + 6F^- \leftrightarrow CrF_6^{3-} + 3e^-$ | $E = E^0 + \frac{2.303RT}{3F}\log\left(\frac{a_{CrF_6^{3-}}}{a_{F^-}^6}\right)$ |
| | 7 | $Cr + 5F^- \leftrightarrow CrF_5^{2-} + 3e^-$ | $E = E^0 + \frac{2.303RT}{3F}\log\left(\frac{a_{CrF_5^{2-}}}{a_{F^-}^5}\right)$ |
| Oxidation of $Cr^{2+}$ fluorides | 8 | $CrF_3^- + 3F^- \leftrightarrow CrF_6^{3-} + e^-$ | $E = E^0 + \frac{2.303RT}{F}\log\left(\frac{a_{CrF_6^{3-}}}{a_{CrF_3^-}a_{F^-}^3}\right)$ |
| | 9 | $CrF_4^{2-} + F^- \leftrightarrow CrF_5^{2-} + e^-$ | $E = E^0 + \frac{2.303RT}{F}\log\left(\frac{a_{CrF_5^{2-}}}{a_{CrF_4^{2-}}a_{F^-}}\right)$ |
| Solvation of chromium fluorides | – | $CrF_3 + 3F^- \leftrightarrow CrF_6^{3-}$ | $\Delta G = \Delta G^0 + 2.303RT\log\left(\frac{a_{CrF_6^{3-}}}{a_{F^-}^3 a_{CrF_3}}\right)$ |
| | – | $CrF_3 + 2F^- \leftrightarrow CrF_5^{2-}$ | $\Delta G = \Delta G^0 + 2.303RT\log\left(\frac{a_{CrF_5^{2-}}}{a_{F^-}^2 a_{CrF_3}}\right)$ |
| Reduction of hydrofluoric acid | 29 | $HF + e^- \leftrightarrow \frac{1}{2}H_2 + F^-$ | $E = E^0 - \frac{2.303RT}{F}\log\left(\frac{p_{H_2}^{1/2}a_{F^-}}{a_{HF}}\right)$ |

**Table 4.** Standard Gibbs free energy of formation ($\Delta G_f^o$) of potassium fluoride and chromium-fluoride compounds at T = 0 Kelvin obtained from various thermodynamic databases.

| Compound | KF | $CrF_2$ | $CrF_3$ | Ref. |
|---|---|---|---|---|
| $\Delta G_f^0$ (kJ/mole) | −569.8 | −777.7 | −1172.7 | Barin[40] |
| | −570.1 | −777.1 | – | Yoo[1] |
| | −562.1 | −721.0 | −1120.7 | OQMD[46,47] |
| | −566.5 | −817.4 | −1174.0 | Jain et al.[34] |

theory cannot completely describe the potential for the quasi-reversible reactions[31].

Before reaching the $CrF_3$ solubility limit in FLiNaK salts, the $CrF_3^-/CrF_6^{3-}$ equilibrium line shows a linearly decreasing potential with $F^-$ ion activity consistent with the prediction of the Nernst equation. When the solubility limit is reached, the ratio of $CrF_3^-$ to $CrF_6^{3-}$ activities is assumed to be 0.0814 calculated assuming the 7.71% conversion shown in Fig. 2b. Therefore, the Nernst potential is a straight horizontal line since an equilibrium ratio was enforced. It is noted that the equilibrium potential of $CrF_3^-/CrF_6^{3-}$ reactions in Fig. 6 is lower than that in Fig. 4a. This is because the $CrF_3^-/CrF_6^3$ activity ratio (Fig. 2b) was considered when constructing the potential $\log(a_{CrF3^-})$ diagram; whereas all Cr ion activities were assumed to be $10^{-6}$ M in Fig. 4a, b.

One observation is that as the $p^{1/2}{}_{H2}/a_{HF}$ ratio increases, the equilibrium potential of $HF/H_2$ reaction decreases and approaches to that of the $CrF_6^{3-}/CrF_3^-$ reduction. As the $CrF_3^-$ activity increases, the stability region of $CrF_3^-$ E-$a_{CrF3-}$ phase space becomes smaller. Practically, based on the estimated $\Delta G_f^0$, the $Cr/CrF_3^-$ boundary will not intersect with that of the $CrF_3^-/CrF_6^{3-}$. Therefore, thermodynamic prediction indicates that the corrosion of Cr may always take place first through the direct dissolution to $Cr^{2+}$ state in the form of $CrF_3^-$, and $CrF_6^{3-}$ will then be formed electrochemically in either within the FLiNaK salts or Cr surface.

### Ramifications towards spontaneous corrosion of Cr in FLiNaK

The diagrams (Figs. 4 and 6) indicate that the KF is oxidized at all potentials where Cr is oxidized to $Cr^{2+}$ and $Cr^{3+}$. The $F^-$ stability region spans the entire region where spontaneous corrosion of Cr occurs. Cr may be oxidized to $Cr^{2+}$ and $Cr^{3+}$ in the presence HF (due to moisture impurity) spontaneously except some extreme combinations of $p^{1/2}{}_{H2}/a_{HF}$ etc. This situation is not changed qualitatively for different solvation of oxidized Cr with $F^-$ and this aspect is substantially similar for the two cases (pair 1: $Cr^0/CrF_3^-/CrF_6^{3-}$; pair 2: $Cr^0/CrF_4^{2-}/CrF_5^{2-}$) considered in this work. Cr may be oxidized by HF and may be oxidized by other sufficiently noble metal impurities (not shown).

It is important to note that Figs. 4 and 6 are conventional thermodynamic stability fields that assume full reversibility of electrochemical reactions, uniform distribution of concentration, and chemical equilibrium between species. Readers must take caution when applying these principles to analyze actual complex corrosion system involving both kinetic and thermodynamic factors. Work is still ongoing to further verify and optimize the accuracy of potential-activity diagrams in molten fluoride salts, for example to theoretically calculate the Gibbs free energy of formation of solvated compounds in molten fluorides. The thermodynamic prediction presented here are consistent with literature the experimental findings of Liu et al.[24] and an ample number of electrochemical studies in FLiNaK salts[14,25,30,35–38]. The potential-activity diagram developed in this work is also useful to help understanding the corrosion thermodynamics and kinetics of metallic alloys in molten fluoride salts, which will be illustrated in our future work.

### Main results

- The Gibbs free energy of formation of $CrF_3^-$, $CrF_4^{2-}$, $CrF_5^{2-}$, and $CrF_6^{3-}$ solvated chromium compounds were extracted from the analysis of cyclic voltammetry data on Pt wire in FLiNaK–$CrF_3$ salts at 600 °C. Based on classical thermodynamics including the Nernst equation, a E-log($a_{F-}$) analogous to a Pourbaix diagram was constructed for two systems: (i) $Cr/CrF_3^-/CrF_6^{3-}$ (ii) $Cr/CrF_4^{2-}/CrF_5^{2-}$ pertinent to Cr exposure in molten fluoride salts.

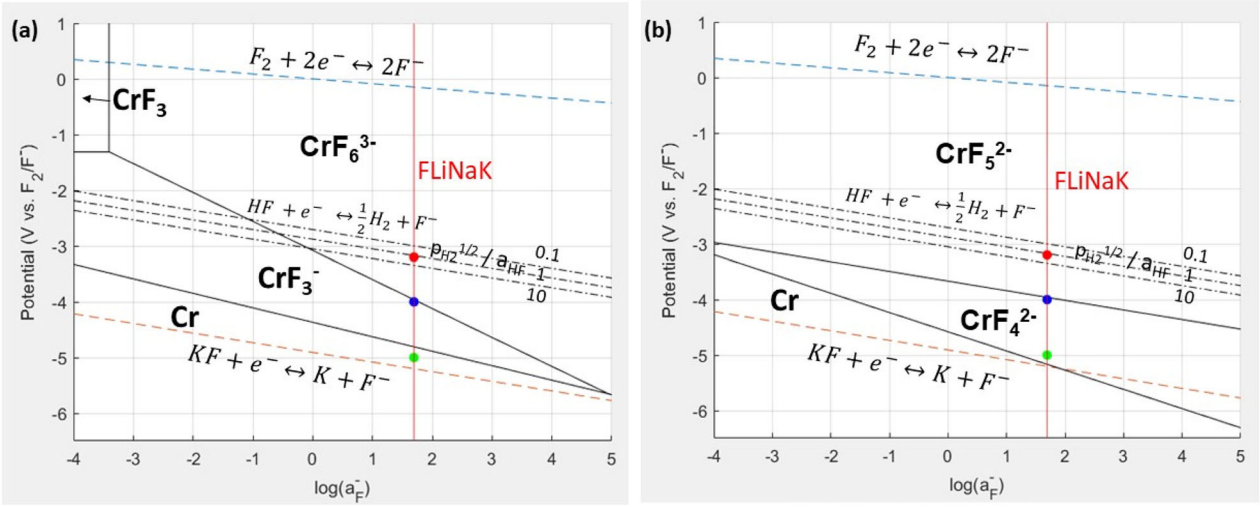


**Fig. 4 Potential log(aF−) equilibrium diagrams for Cr. a** Considers the $CrF_3^-$ and $CrF_6^{3-}$ species and (**b**) the $CrF_4^{2-}$ and $CrF_5^{2-}$ solvated states. The red, blue, and green dots at log($a_F^-$) = 1.693 mark the potentials for XRD results presented in Fig. 6. All Cr–F species were assumed to have an activity of $10^{-6}$ M.

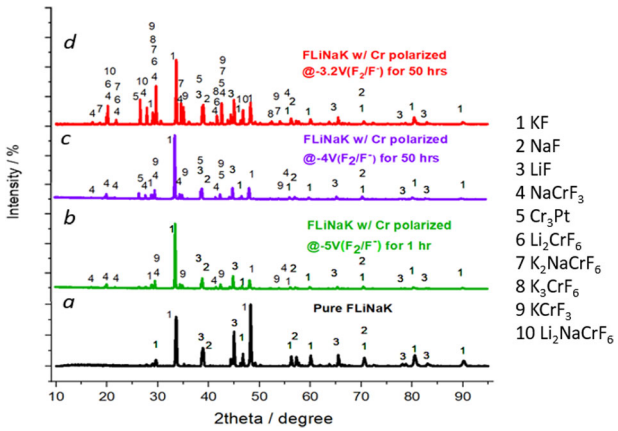


**Fig. 5 X-ray diffractogram of the solidified FLiNaK salt at room temperature.** (**a**) displays the diffractogram baseline condition without Cr, and with Cr potentiostatically polarized to (**b**) −5 $V_{F_2/F^-}$ for 1 h, (**c**) −4 $V_{F_2/F^-}$ for 50 h, (**d**) −3.2 $V_{F_2/F^-}$ for 50 h.

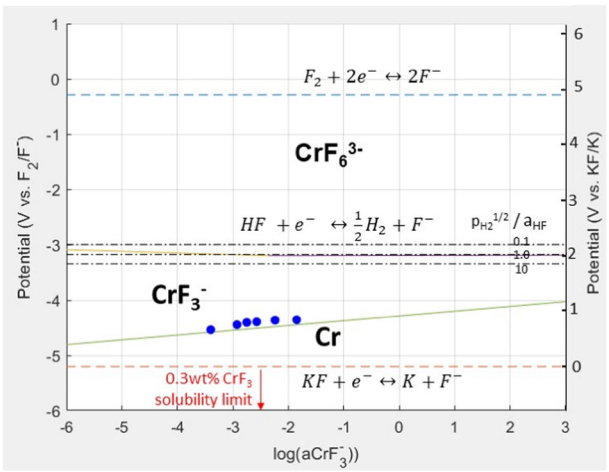


**Fig. 6 Potential-log(a$CrF_3^-$) equilibrium diagram for Cr in FLiNaK salts (log($a_F^-$) = 1.693) at 600 °C.** The blue dot indicates the experimental equilibrium redox potential of the $Cr/Cr^{2+}$ half-cell reactions reported in Fig. 4.

- To validate the prediction, a Cr coupon was potentiostatically held at selected potentials corresponding to the different thermodynamic stability regions, and the solidified salts were analyzed using X-ray diffraction. Experimental XRD results confirmed that the $Cr/CrF_3^-/CrF_6^{3-}$ described Cr corrosion thermodynamics in FLiNaK salts at 600 °C, while $CrF_4^{2-}$ or $CrF_5^{2-}$ compounds were not detected by XRD.
- A E-log($a_{CrF_3^-}$) diagram based on the $Cr/CrF_3^-/CrF_6^{3-}$ system was also developed to predict the most thermodynamically favorable oxidation state for Cr corrosion. The prediction shows that the direct dissolution from Cr to $CrF_3^-$ via a +2 charge is favored over all reasonable values of $a_{HF}$. $F^-$ complexation assuming $Cr/CrF_3^-/CrF_6^{3-}$ compared to $CrF_4^{2-}$ or $CrF_5^{2}$ produces E-$a_{HF}$ diagrams which are similar but have distinct differences.
- The E-log(aF-) diagram indicates that the K is oxidized to $K^+$ existing as KF at all potentials where Cr is oxidized to $Cr^{2+}$ and $Cr^{3+}$. The $F^-$ stability region spans the entire region where spontaneous corrosion of Cr occurs. Cr may be oxidized to $Cr^{2+}$ and $Cr^{3+}$ in the presence HF (due to moisture impurity) spontaneously except for some conditions of $p^{1/2}{}_{H2}/a_{HF}$ etc.

This situation is not changed qualitatively for various states of solvation between oxidized Cr solute in $F^-$ solvent and this aspect is similar for the two cases (pair 1: $Cr^0/CrF_3^-$/ $CrF_6^{3-}$; pair 2: $Cr^0/CrF_4^{2-}/CrF_5^{2-}$) considered in this work.

## METHODS

### Setup, sample, and salt preparation

High purity Cr rectangular sheet (99.995%, Alfa Aesar) with the dimension 20 × 1.5 × 3 mm were used. Coupons were metallographically prepared to 1200 grit surface finish using silicon carbide polishing papers. The FLiNaK salt was prepared by weighing LiF (99.85%, Fisher Scientific), NaF (99.99%, Fisher Scientific), KF (99.5%, Fisher Scientific) into the stoichiometric ratio of 46.5, 11.5, and 42 mol%, respectively. Prior to mixing, these salts were dried in a vacuum furnace for 48 h at 100 °C, and then transferred to a $N_2$-filled glove box with controlled $O_2$ and $H_2O$ levels below <0.1 ppm. Nevertheless, during this transfer process, it is expected that the salts could absorb water from moist air during transfer (relative humidity of the laboratory was about 30%). In all, 30 g of FLiNaK salt were used for each experiment. The mass

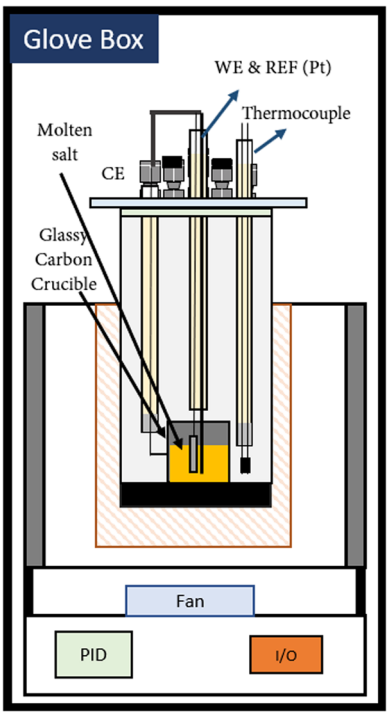


**Fig. 7** Schematics of the experimental setup used for molten salt electrochemical characterization.

ratio of salt to Cr coupon is approximately equivalent to 0.03 g of FLiNaK/g of Cr.

The setup to perform electrochemical measurement is shown in Fig. 7. All measurements were carried out in a $N_2$-filled glove box in a modified muffle furnace at 600 °C. A glassy carbon crucible (99.999%, Fisher Scientific) was used as both the salt container and counter electrode, and a Pt wire was used as a Pt/PtO/$O^{2-}$ quasi-reference electrode based on a controlled oxygen level. The working electrode was either a Cr coupon spot welded to a Ni200 wire or a platinum wire (99.997%, Alfa Aesar™). All the electrodes were fed through an alumina tube and placed in a quartz tube to ensure sturdy connections. A Gamry interface 1000 potentiostat was used to perform electrochemical tests. To minimize impurities pertaining to residual water moisture or oxygen, prior to the insertion of test electrodes, the salt mixture was heated to 600 °C for 3 h under the flow of ultra-high purity $N_2$ gas (99.999%).

## Reference potential determination

For a more meaningful and reliable comparison between thermodynamic prediction and electrochemistry results, the electrode potential was represented relative to both the potassium fluoride reduction (reaction 27, KF/K) and fluorine gas evolution (reaction 28, $F_2/F^-$).

The redox potential for reaction 27 can be experimentally measured using a cyclic voltammetry technique performed on a Pt wire in molten fluoride salts[27]. This method has also been utilized by Massot et al.[27], Shay et al.[42], and Wang et al.[33]. The technique involves polarizing the Pt wire to a cathodic (negative) direction until a sharp increase in reduction current corresponding to KF reduction is detected, and the scan is reversed to oxidize the K deposited on the Pt wire surface. An example cyclic voltammogram is shown in Fig. 1a. The equilibrium potential of reaction 27 was estimated at the position between the oxidation peak (KF/K). Once the KF/K potential was known, the $F_2/F^-$ potential was be calculated using the Nernst equation (in FLiNaK salts where $\log(a_{F^-}) = 1.693$, $E_{KF/K} = -5.206\ V_{F_2/F^-}$).

## Thermodynamic analysis

In this project, a systematic thermodynamic analysis was carried out to predict the most favorable reaction for Cr dissolution as a function of potential and fluoride ion activities. Firstly, consider a general, reversible, half-cell electrochemical reaction in molten fluorides as shown:

$$M + xF^- \leftrightarrow MF_x^{n-x} + ne^- \tag{30}$$

where x describes the number of fluoride ions reacted per atom of Cr. The Nernst Equation for reaction 30 can be represented by the Nernst equations as[43]:

$$E_{M/MF_x^{n-x}} = E^0_{M/MF_x^{n-x}} + \frac{2.303RT}{nF}\log\left(\frac{a_{MF_x^{n-x}}}{a_{F^-}^x a_M}\right) \tag{31}$$

$$E_{M/MF_x^{n-x}} = E^0_{M/MF_x^{n-x}} + \frac{0.173}{n}\log\left(\frac{a_{MF_x^{n-x}}}{a_{F^-}^x a_M}\right) \tag{32}$$

where $E_{M/MF^{x+}}$ is the Nernst potential (or equilibrium redox potential), R is the universal gas constant, $T$ is the temperature in K, $n$ is the number of electrons transferred to complete the reaction shown one time, F is the Faraday's constant of 96,500 coulombs/mol of e-, $a_i$ ($=\gamma_i C_i$) is the ion activity, and $E^0_{M/MF_n^{x+}}$ is the standard electrode potential of the half-cell reaction. The $E^0_{M/MF_n^{x+}}$ can be related to $\Delta G_f^0$ through Eqs. (17) and (18) (see introduction).

Table 1 shows the $\Delta G_f^0$ of potassium and chromium-fluoride compounds obtained from Barin et al.[40]. Since the melting point of KF, $CrF_2$, $CrF_3$ is higher than 600 °C, the $\Delta G_f^0$ at supercooled state was used instead. This is calculated by the summation of their solid state $\Delta G_f^0$ and the fusion energy ($\Delta G_F^0$)[6,44] obtained by the following equations:

$$\Delta G_F^0 = (H_{l,F}^0 - H_{s,F}^0) - T(S_{l,F}^0 - S_{s,F}^0) \tag{33}$$

where the subscript "l" is liquid phase and "s" is solid phase. The values of $H_{l,F}^0$, $H_{s,F}^0$, $S_{l,F}^0$, $S_{s,F}^0$ values were obtained from the FactSage 8.0 SGTE pure substances database (v13.1)[45]. It is noted that the $\Delta G_f^0$ of fluoride ion ($F^-$) is assumed to be 0 and the partial pressure of fluorine gas ($F_2$) is assumed to be 1 atm so reaction 28 can be a reference for other electrochemical reactions. To ensure the reliability of the $\Delta G_f^0$ values used in this work, the $\Delta G_f^0$ values from various thermodynamic databases are listed in Table 4. It is noted that these values represent the condition at $T = 0$ K. The $\Delta G_f^0$ values from Barin et al.[40] are consistent with Yoo[1] and with two open source thermodynamic databases: Open Quantum Materials Database (OQMD)[46,47] and Materials Project (MP)[34]. The method to convert the formation energy reported in OQMD and MP, from eV/atom to the standard unit of kJ/mol, can be found in the work of Lany et al[48].

To predict the thermodynamic stability of Cr, the equilibrium redox reactions that are possible involving the $Cr^0$, $CrF_3$, $CrF_3^-$, $CrF_4^{2-}$, $CrF_5^{2-}$, $CrF_6^3$ species must be considered. Table 3 lists the possible redox reactions and their Nernst equations. The potential window offered by molten fluorides can be defined by the reduction of potassium fluoride (reaction 27) and fluorine gas evolution (reaction 28). The Nernst potentials of possible redox reactions are computed as a function of electrochemical potential and fluoride ion activity. These results are presented in the form of a potential-activity diagram (vs. $\log(a_{F^-})$ and $\log(a_{CrF_3^-})$) applicable for molten fluoride salt, which is analogous to Pourbaix diagram developed for aqueous systems[28].

## Estimating the Gibbs free energy of solvated chromium-fluoride ions

To perform a complete thermodynamic analysis, the Gibbs free energy of formation ($\Delta G_f^0$) of various chromium-fluoride compounds (e.g. $CrF_3^-$, $CrF_4^{2-}$, $CrF_5^{2-}$, $CrF_6^{3-}$) needs to be known. However not all of these values are reported in the literature. In this work, an electrochemical method was used to determine the $\Delta G_f^o$ values of these compound[27]. The redox electrode potentials ($E_{M/MF_x^{n-x}}$) of Cr redox reactions (4–9) was determined from cyclic voltammetry performed on a platinum wire inserted in FLiNaK salts with the addition between 0.11 and 1 wt% of $CrF_3$ (97%, Fisher Scientific) at 600 °C. The standard electrode potential ($E^0_{M/MF^{n-x}}$) was obtained by the extrapolation of $E_{M/MF_x^{n-x}}$ to 1 M $MF_x^{n-x}$ in the FLiNaK salts. The $\Delta G_f^0$ of possible chromium-fluoride compounds were calculated using Eq. 17[27].

## Potentiostatic test and X-ray diffraction

To access the validity of thermodynamic predictions, a pure Cr coupon was potentiostatically polarized to $-3.2\ V_{F_2/F^-}$ for 50 h, $-4\ V_{F_2/F^-}$ for 50 h, $-5\ V_{F_2/F^-}$ for 1 h in FLiNaK salts at 600 °C using a Pt qusai-reference electrode and a glassy carbon crucible as a counter electrode. The details for the electrochemical setup is presented in the section "Setup, sample and salt preparation".The phase composition of solidified salts was analyzed by

XRD using the Malvern–Panalytical Empyrean diffractometer [wavelength Cu Kα (1.5405 A)]. The PDF4+ database was used as the reference data. The software HighScore Plus was used for Rietveld refinements. The peak profile was refined by pseudo-Voigt function.

## DATA AVAILABILITY

The authors declare that the data supporting the findings of this study are available within the paper. The supplementary data will be available upon reasonable request.

Received: 31 October 2021; Accepted: 28 April 2022;
Published online: 09 June 2022

## REFERENCES

1. Yoo, J. H. *Thermodynamic Data-Base for Metal Fluorides*, Technical Report Number: TR-1824, (Korea Atomic Energy Research Institute) KAERI, (2001).
2. Dolan, T. J. *Molten Salt Reactors and Thorium Energy* (Woodhead Publishing, 2017).
3. Serp, J. et al. The molten salt reactor (MSR) in generation IV: overview and perspectives. *Prog. Nucl. Energy* **77**, 308–319 (2014).
4. Wright, R. N. & Sham, T. L. Status of Metallic Structural Materials for Molten Salt Reactors. Technical Report INL/EXT-18-45171; Argonne National Laboratory & Idaho National Laboratory (2018).
5. Busby, J. et al. *Technical Gap Assessment for Materials and Component Integrity Issues for Molten Salt Reactors*. Technical Report ORNL/SPR-2019/1089; Oak Ridge National Laboratory (2019).
6. Guo, S. et al. Corrosion in the molten fluoride and chloride salts and materials development for nuclear applications. *Prog. Mater. Sci.* **97**, 448–487 (2018).
7. Sridharan, K. & Allen, T. *Molten Salts Chemistry from Lab to Application - Chapter 12: Corrosion in Molten Salts* (Elsevier, 2013).
8. Zhang, J. et al. Redox potential control in molten salt systems for corrosion mitigation. *Corros. Sci.* **144**, 44–53 (2018).
9. Baes, C. F. The chemistry and thermodynamics of molten salt reactor fuels. *J. Nucl. Mater.* **51**, 149–162 (1974).
10. Winner, N. et al. Ab-initio simulation studies of chromium solvation in molten fluoride salts. *J. Mol. Liq.* **335**, 116351 (2021).
11. Wang, Y. et al. Effects of the oxidants $H_2O$ and $CrF_3$ on the corrosion of pure metals in molten (Li,Na,K)F. *Corros. Sci.* **103**, 268–282 (2016).
12. Pizzini, S. & Morlotti, R. Oxygen and hydrogen electrodes in molten fluorides. *Electrochim. Acta* **10**, 1033–1041 (1965).
13. Ai, H. et al. Effects of $O_2$—additive on corrosion behavior of Fe–Cr–Ni alloy in molten fluoride salts. *Corros. Sci.* **150**, 175–182 (2019).
14. Wu, W. et al. Electrochemical behaviors of Cr(III) in molten LiF-NaF-KF eutectic. *Int. J. Electrochem. Sci.* **13**, 225–234 (2018).
15. Yoko, T. & Bailey, R. A. Electrochemical studies of chromium in molten LiF - NaF - KF (FLINAK). *J. Electrochem. Soc.* **131**, 2590–2595 (1984).
16. Jordan, W. H. et al. *Aircraft Nuclear Propulsion Project Quarterly Progress Report*. Technical Report Number: ORNL-2221; Oak Ridge National Laboratory (1957).
17. Koger, J. W. *Effect of $FeF_2$ Addition on Mass Transfer in A Hastelloy N: LiF-$BeF_2$-$UF_4$ Thermal Convection Loop System*. Technical Report Number: ORNL-TM-4188; Oak Ridge National Laboratory (1972).
18. DeVan, J. H. & Evans, III, R. B. *Corrosion Behavior of Reactor Materials in Fluoride Salt Mixtures*. Technical Report ORNL-TM-328; Oak Ridge National Laboratory (1962).
19. Jordan, W. H. et al. *Aircraft Nuclear Propulsion Project Quarterly Progress Report for Period Ending Sept. 10, 1956*. Technical Report Number: ORNL-2157; Oak Ridge National Laboratory (1956).
20. Song, Y. et al. Solubility of $Cr_2O_3$ in molten fluorides with different $ZrF_4$ contents and fluoroacidities. *J. Electrochem. Soc.* **167**, 023501 (2020).
21. Qiu, J. et al. Electrochemical study of the dissolution of oxide films grown on type 316L stainless steel in molten fluoride salt. *Corros. Sci.* **186**, 109457 (2021).
22. Wang, Y., Liu, H., Yu, G., Hou, J. & Zeng, C. Electrochemical study of the corrosion of a Ni-based alloy GH3535 in molten (Li,Na,K)F at 700 °C. *J. Fluor. Chem.* **178**, 14–22 (2015).
23. Zhou, W. et al. Proton irradiation-decelerated intergranular corrosion of Ni-Cr alloys in molten salt. *Nat. Commun.* **11**, 3430 (2020).
24. Liu, Y. et al. Corrosion of Cr in molten salts with different fluoroacidity in the presence of $CrF_3$. *Corros. Sci.* **169**, 108636 (2020).
25. Wang, Y. & Zhang, J. Electrochemical properties of $CrF_2$ in FLiNaK molten salt and the new analytical methods for their determination. *J. Electrochem. Soc.* **167**, 086503 (2020).
26. Cramer, S. D. & Covino Jr., B. S. *ASM Handbook Volume 13A: Corrosion: Fundamentals, Testing, and Protection* (ASM International, 2003).
27. Massot, L. et al. Corrosion products electrochemical behaviour into molten lif-naf: investigation of Cr(II) system. *J. Electrochem. Soc.* **168**, 026510 (2021).
28. Pourbaix, M. *Atlas of Electrochemical Equilibria in Aqueous Solutions* (National Association of Corrosion Engineers, 1974).
29. Sohal, M. S. et al. *Engineering Database of Liquid Salt Thermophysical and Thermochemical Properties*. Technical Report Number: INL/EXT-10-18297; Idaho National Laboratory (2010).
30. Ludwig, D. et al. High temperature electrochemistry of molten fluoride salt for measurement of dissolved chromium. *Corros. Eng., Sci. Technol.* **46**, 360–364 (2011).
31. Elgrishi, N. et al. A practical beginner's guide to cyclic voltammetry. *J. Chem. Educ.* **95**, 197–206 (2018).
32. Hamman, C. H. et al. *Electrochemistry*, 2nd edition. (Wiley, 2007).
33. Wang, Y. *Species Chemistry and Electrochemical Separation in Molten Fluoride Salt*. PhD's thesis, Virginia Polytechnic Institute and State University (2019).
34. Jain, A. et al. The materials project: a materials genome approach to accelerating materials innovation. APL. *Materials* **1**, 011002 (2013).
35. Zakharova, V. V. et al. Electrochemistry of iron, nickel and chromium in LiF–NaF–KF (FLiNaK) eutectic melt: a cyclic voltammetry study. *AIP Conf. Proc.* **2313**, 050039 (2020).
36. Peng, H. et al. Electrochemical investigation of the stable chromium species in molten FLINAK. *RSC Adv.* **5**, 76689–76695 (2015).
37. Zheng, G. & Sridharan, K. Corrosion of structural alloys in high-temperature molten fluoride salts for applications in molten salt reactors. *JOM* **70**, 1535–1541 (2018).
38. Doniger, W. H. & Sridharan, K. Application of voltammetry for quantitative analysis of chromium in molten 2LiF-$BeF_2$ (FLiBe) salt. *J. Electrochem. Soc.* **838**, 73–81 (2019).
39. Yin, H. et al. Thermodynamic modeling of LiF-NaF-KF-CrF3 system. *J. Fluor. Chem.* **209**, 6–13 (2018).
40. Barin, I., Knacke, O. & Kubaschewski, O. *Thermochemical Properties of Inorganic Substances* (Springer Berlin Heidelberg, 1977).
41. Bieber, A. L. et al. Fluoroacidity evaluation in molten salts. *Electrochim. Acta* **6**, 5022–5027 (2011).
42. Shay, N. W. *Electrochemical Sensor Development for Fluoride Molten Salt Redox Control*. Master's thesis, Ohio State University (2017).
43. Jones, D. A. *Principles and Prevention of Corrosion* (Prentice Hall, 1996).
44. Guo, S., Shay, N., Wang, Y., Zhou, W. & Zhang, J. Measurement of europium (III)/europium (II) couple in fluoride molten salt for redox control in a molten salt reactor concept. *J. Nucl. Mater.* **496**, 197–206 (2017).
45. Bale, C. W. et al. FactSage thermochemical software and databases—recent developments. *CALPHAD* **33**, 295 (2009).
46. Saal, J. E. et al. Materials design and discovery with high-throughput density functional theory: the open quantum materials database (OQMD). *JOM* **65**, 1501–1509 (2013).
47. Kirklin, S. et al. The open quantum materials database (OQMD): assessing the accuracy of DFT formation energies. *npj Comput Mater.* **1**, 1–15 (2015).
48. Stevanović, V. et al. Correcting density functional theory for accurate predictions of compound enthalpies of formation: fitted elemental-phase reference energies. *Phys. Rev. B* **85**, 115104 (2012).

## ACKNOWLEDGEMENTS

Research primarily was supported as part of fundamental understanding of transport under reactor extremes (FUTURE), an Energy Frontier Research Center (EFRC) funded by the U.S. Department of Energy (DOE), Office of Science, Basic Energy Sciences (BES). This work was performed in the Department of Materials Science and Engineering (DMSE) in the Center for Electrochemical Science and Engineering (CESE) at the University of Virginia. Utilization of the Malvern–Panalytical Empyrean diffractometer were supported by Nanoscale Materials Characterization Facility (NMCF) with National Science Foundation (NSF) under award CHE-2102156.

## AUTHOR CONTRIBUTIONS

H.L.C. and E.R. conceived the methodology to obtain the needed thermodynamic data and designed the experiments to obtain free energies of formation and Nernst potentials. H.L.C., E.R., and J.Q. performed the experimental analysis. H.L.C. was responsible for thermodynamic analysis and diagrams construction and prepared the original draft with input from J.R.S and E.R. J.R.S. guided application of corrosion thermodynamic criteria for spontaneous corrosion with H.L.C. and E.R., edited and reviewed the manuscript. J.R.S. and P.H. conceptualized and directed the project. P.H. was responsible for funding acquisition and overall project themes within F.U.T.U.R.E. All the authors contributed to the interpretation of the experimental data and discussed the results. All authors discussed the data interpretation. All co-authors contributed during reviewing of the final manuscript. All authors approved the final version.

## COMPETING INTERESTS

The authors declare no competing interests.

## ADDITIONAL INFORMATION

**Correspondence** and requests for materials should be addressed to Ho Lun Chan or Elena Romanovskaia.

**Reprints and permission information** is available at http://www.nature.com/reprints

**Publisher's note** Springer Nature remains neutral with regard to jurisdictional claims in published maps and institutional affiliations.